



# 1 Hydrogeological controls on the spatio-temporal variability of surge- 2 induced hydraulic gradients along coastlines: implications for beach 3 surface stability

4 Anner Paldor<sup>1</sup>, Nina Stark<sup>2</sup>, Matthew Florence<sup>2</sup>, Britt Raubenheimer<sup>3</sup>, Steve Elgar<sup>3</sup>, Rachel Housego<sup>3,4</sup>,  
5 Ryan S. Frederiks<sup>1</sup>, Holly A. Michael<sup>1,5</sup>

6 <sup>1</sup> Department of Earth Sciences, University of Delaware, Newark, DE, USA.

7 <sup>2</sup> Department of Civil and Environmental Engineering, Virginia Polytechnic Institute and State University, Blacksburg, VA,  
8 USA.

9 <sup>3</sup> Department of Applied Ocean Physics and Engineering, Woods Hole Oceanographic Institution, Woods Hole, MA, USA.

10 <sup>4</sup> MIT-WHOI Joint Program in Oceanography, 86 Water St., Woods Hole, MA, USA.

11 <sup>5</sup> Department of Civil and Environmental Engineering, University of Delaware, Newark, DE, USA.

12 *Correspondence to:* Holly A. Michael ([hmichael@udel.edu](mailto:hmichael@udel.edu))

13 **Abstract.** Ocean surges pose a global threat for coastal stability. These hazardous events alter flow conditions and pore  
14 pressures in flooded beach areas during both inundation and subsequent retreat stages, which can mobilize beach material,  
15 potentially enhancing erosion significantly. In this study, the evolution of surge-induced pore-pressure gradients is studied  
16 through numerical hydrologic simulations of storm surges. The spatiotemporal variability of critically high gradients is  
17 analyzed in 3D. The analysis is based on a threshold value obtained for momentary liquefaction of beach materials under  
18 groundwater seepage. Simulations of surge events show that during the run-up stage, head gradients can rise to the calculated  
19 critical level landward of the advancing inundation line. During the receding stage, critical gradients were simulated seaward  
20 of the retreating inundation line. These gradients reach maximum magnitudes just as sea level returns to pre-surge level, and  
21 are most accentuated beneath the still-water shoreline, where the model surface changes slope. The gradients vary along the  
22 shore owing to variable beach morphology, with the largest gradients seaward of intermediate-scale (1-3m elevation)  
23 topographic elements (dunes) in the flood zone. These findings suggest that the common practices in monitoring and mitigating  
24 surge-induced failures and erosion, which typically focus on the flattest areas of beaches, might need to be revised.



## 25 **1 Introduction**

26 Groundwater seepage can destabilize land areas, especially at the interface between terrestrial and submerged systems  
27 (Iverson, 1995; Iverson & Major, 1986; Iverson & Reid, 1992; Schorghofer et al., 2004; Stegmann et al., 2011). Recent studies  
28 have examined the characteristics of pore pressure behavior, the associated groundwater seepage, and its effect on the stability  
29 of geomaterials (soils, rocks, etc.), including field observations (Mory et al., 2007; Sous et al., 2016), physical experiments  
30 (Schorghofer et al., 2004; Sous et al., 2013), numerical simulations (Orange et al., 1994; Rozhko et al., 2007; Schorghofer et  
31 al., 2004), and analytical models (Sakai et al., 1992; Yeh & Mason, 2014). There are several examples of seepage-induced  
32 failure of the surface (i.e. the mobilization of the soil skeleton) from around the world, including Japan (Yeh & Mason, 2014),  
33 California (Orange et al., 2002), and France (Sous et al., 2016; Stegmann et al., 2011).

34 Soil liquefaction occurs when pore pressures in the geomaterial rise to a point where its effective stress drops to zero and the  
35 material is fluidized, and thus acts as a liquid. At the coast, ocean (waves, surge, tides, inundation) and terrestrial (groundwater  
36 heads, precipitation, and overland flows) processes concurrently contribute to changing pore pressures in beach and nearshore  
37 sediments, and changes in pore pressure distributions and gradients could induce failure of the surface. Ocean effects on pore  
38 pressures, groundwater flow, and seepage occur due to wind waves, storm surges, and tsunamis. For example, a 1D analytical  
39 model suggests that during a tsunami, vertical hydraulic gradients can destabilize sediments and increase the potential for  
40 sediment momentary liquefaction, consistent with laboratory experiments (Abdollahi & Mason, 2020; Yeh & Mason, 2014).  
41 Laboratory experiments (Sous et al., 2013) suggest that the magnitude of hydraulic gradients in the beach due to infiltration  
42 from sea-swell and infragravity waves depend on the wave frequency, cross-shore position, water table overheight, and the  
43 presence of standing waves. A large-scale (250 m) flume study of a barrier island showed that waves can alter the coastal  
44 groundwater head distribution significantly, and can change cross-island and local (under the ocean beach) hydraulic gradient  
45 directions (Turner et al., 2016). Field observations of pore-pressures over several tidal cycles in a microtidal beach (Sous et  
46 al., 2016) suggest that breaking-wave-driven onshore increases in the water surface (setup) over the 10 m nearest the shoreline  
47 induced groundwater head changes of  $O(0.1 \text{ m})$  (Sous et al., 2016). Furthermore, density-driven flow at the subsurface  
48 transition zone between fresh terrestrial groundwater and saline groundwater can produce intense, localized seepage (Burnett  
49 et al., 2006). Rapid changes in seepage characteristics (locations, magnitudes, direction) during extreme events may lead to  
50 sediment liquefaction (i.e., loss of particle-to-particle contacts and sediment effective stresses) and mobilization, resulting in  
51 erosion and structure destabilization.

52 Observations, theories, and simulations have shown that the pore-pressure changes owing to energetic ocean waves can reduce  
53 effective stresses and may cause liquefaction (Chini & Stansby, 2012; Mory et al., 2007; Sakai et al., 1992; Sous et al., 2013;  
54 Yeh & Mason, 2014). Measured pore-pressure changes in beach sediments during intense waves suggest that momentary  
55 liquefaction may occur at shallow depths ( $<1 \text{ m}$ ) below the surface (Mory et al., 2007), consistent with theory (Sakai et al.,  
56 1992). Analytical solutions for the effective stress in an idealized seabed suggest that waves can alter the stresses in the upper  
57 meters of the seafloor significantly (Mei & Foda, 1981; Sakai et al., 1992). Simulations of a theoretical 2D porous medium,



58 where an increase in pore pressure is applied at the bottom of the layer from a point source, revealed that different spatial  
59 failure patterns (i.e. the geometry of the slip surface) can occur under various stress regimes (i.e. distribution of stresses in the  
60 soil) (Rozhko et al., 2007), although the process that leads to the simulated change in the pore-pressure distribution was  
61 unexplored.

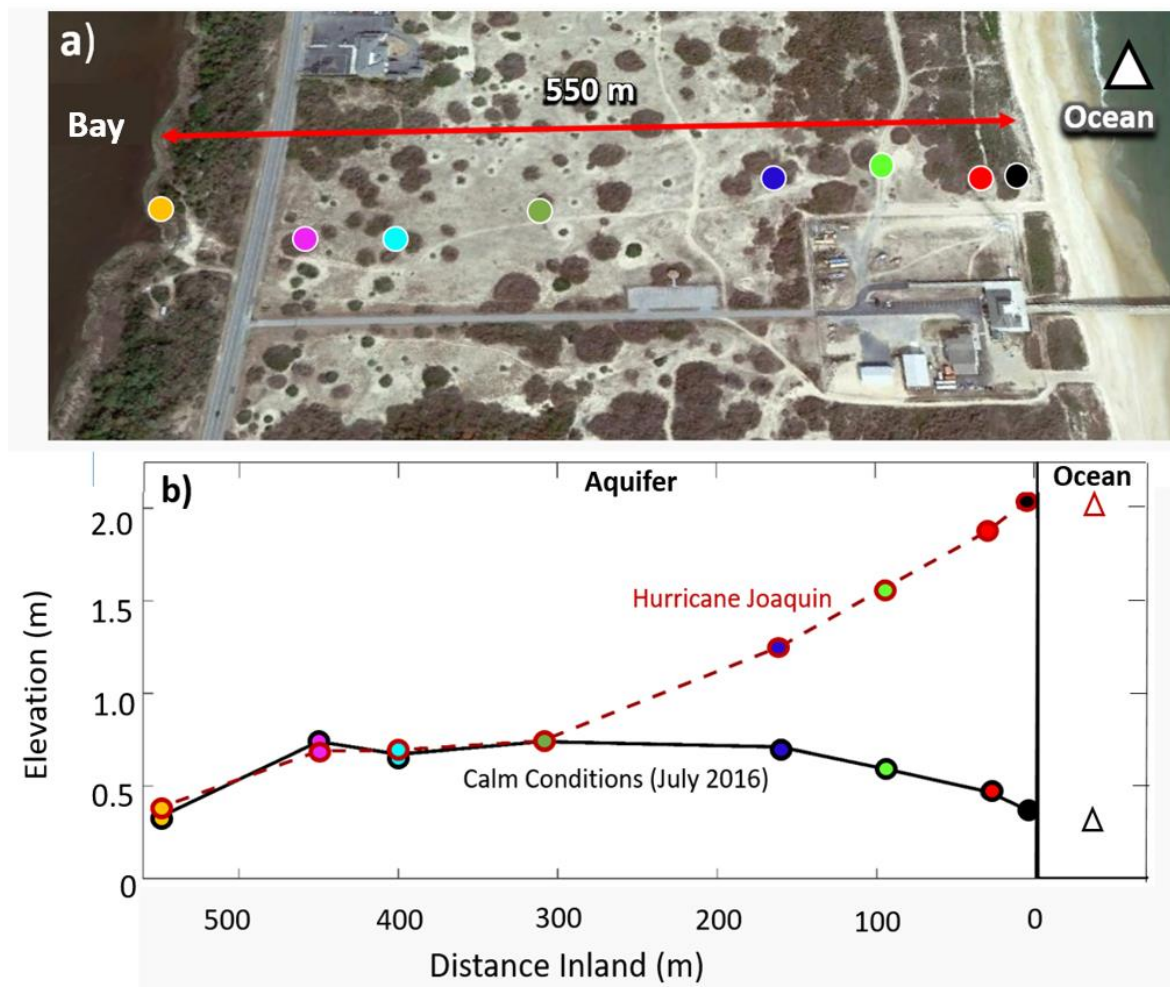
62 Apart from waves, storm surges also could alter the onshore hydrogeological regime and potentially reduce the stability of the  
63 beach surface, yet surges have not been explored in this context. This work focuses on the influence of alongshore topography  
64 and hydrogeological factors on geotechnical impacts near the shoreline owing to ocean surges driven by coastal storms, which  
65 are projected to intensify and become more frequent in the future (Chini & Stansby, 2012; Tebaldi et al., 2012). In particular,  
66 the three-dimensional dynamics of surge-induced inundation and the resulting shore-parallel distribution of pore-pressure  
67 gradients in sandy beach areas are not well understood. Specific questions addressed in this work are: (1) Can surge-induced  
68 pore pressure changes promote sediment liquefaction of the uppermost sediment layers (<5 m), and which areas across the  
69 beach are the most vulnerable? (2) What is the relationship between beach morphology and the spatio-temporal evolution of  
70 pore pressure gradients? (3) How do the hydrogeological properties (hydraulic conductivity, groundwater recharge) of the  
71 coastal system affect the potential for failure? Field evidence is presented for the effect of storm surges on coastal groundwater  
72 heads (Section 2), a criterion is derived (Section 3) for momentary soil liquefaction for beach slopes with groundwater  
73 discharge based on existing solutions (Briaud, 2013), and a model framework is described (Section 4) and used to simulate  
74 surges in theoretical beach settings and to examine their effect on sediment stability (Section 5).

## 75 **2 Field evidence for hydraulic head changes during storm surges**

76 Groundwater observations collected every 10 min from October 2014 to November 2017 in 8 wells deployed across a 500-m  
77 wide barrier island on the Outer Banks of NC, near the town of Duck (Figure 1a) indicate that coastal storm waves and surge  
78 significantly affect the freshwater equivalent heads from the beach to more than 310 m inland of the beach (Housego et al.,  
79 2018). The study period included 27 storm events (including 4 hurricanes) in which wave heights measured in 26-m water  
80 depth (NDBC Station 44100) often exceeded 3.5 m, surge (NOAA tide gauge 8651371) was between 0.5 and 1.0 m, and 36-  
81 hr-averaged (to remove fluctuations owing to tides and wind wave motions) shoreline water levels increased from about 0.6  
82 to 2.4 m owing to surge and wave-driven setup (included in the simulated surge height). In response to the increased ocean  
83 water levels, the groundwater level under the ocean dunes rose 0.5 to 2.0 m. For example, following the passage of Hurricane  
84 Joaquin in 2015, which caused offshore wave heights of 4.7 m ( and <1 cm of rainfall), head levels under the ocean dunes and  
85 25, 90, 160, and 310 m farther inland increased 1.6, 1.4, 1.2, 0.9, and 0.5 m above pre-storm levels, respectively (Figure 1b).  
86 These and other storm-driven increases in head levels changed the direction of the hydraulic gradient from toward the bay  
87 (inland) during calm conditions to toward the ocean during storms (compare black and red points in Figure 1b under calm  
88 conditions with those during the storm). After the shoreline water level returns to pre-storm conditions, the water table behind  
89 the dune remains elevated and groundwater discharges back out through the beach as the water table recovers. During the



90 storm, the horizontal location of the shoreline remained more than 10 m seaward of the dunes, and thus there was no inundation  
91 from overtopping, which could increase groundwater levels even farther inland. Changes in hydraulic gradients, including the  
92 effects of inundation, are investigated in Section 4 with a numerical model that does not mimic the conditions in this field site,  
93 but is a generalized representation of coastal hydrogeological systems.



94

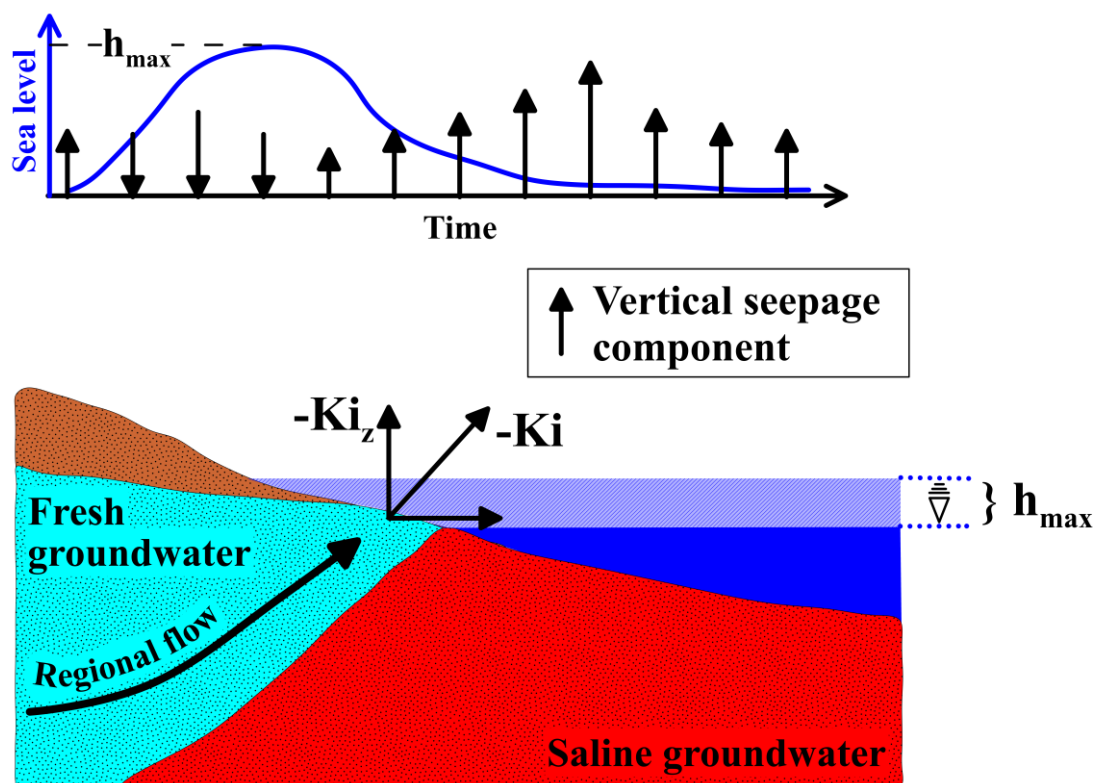
95 **Figure 1:** a) © Google Earth image of the Outer Banks near Duck, NC, with the locations of groundwater wells (colored circles). (b)  
96 Elevation of the ocean level (triangles) and 36 hr-avg. freshwater equivalent groundwater heads (circles) vs. inland distance from  
97 the dune ( $x=0$  m). Colors correspond to colors of symbols in (a) for the average of the calm conditions in July 2016 (black triangle  
98 and circle outlines connected by black lines) and at the peak of Hurricane Joaquin (red triangle and circle outlines connected by red  
99 dashed lines).

100



### 101 **3 Conceptual model and governing equations**

102 A conceptual model of a coastal system (Figure 2) includes infiltration of rain that recharges the aquifer with freshwater,  
103 resulting in fresh groundwater flow toward the ocean. In the nearshore area (typically within meters of the shoreline), an  
104 inclined freshwater-saltwater transition zone develops between the saline groundwater underlying the seafloor and the  
105 terrestrial fresh groundwater. The density gradient at the transition zone deflects the fresh groundwater flow upward, and  
106 produces focused groundwater discharge near the coastline that can be amplified by an order of magnitude or more relative to  
107 the average flow rate in the aquifer (Paldor et al., 2020). In phreatic aquifers, submarine groundwater discharge typically occurs  
108 within tens of meters of the coastline, depending on the recharge rates and aquifer properties (Bratton, 2010). In systems where  
109 the discharge is into a body of freshwater (e.g., a lake), the bottom of the lake is a constant head boundary, and thus the seepage  
110 is, by definition, perpendicular to the lakebed. This assumption is widely adopted in geotechnical calculations of groundwater  
111 discharge magnitudes. For example, in flow net solutions for classic dam and levee problems, the bottom of the river on both  
112 sides of the dam or levee is considered an equipotential line (Briaud, 2013). However, along the bottom of a saltwater body  
113 the freshwater-equivalent head is variable with bathymetry, and hence the seepage is not necessarily perpendicular to the  
114 seafloor and possibly represents a complex, three-dimensional problem with high spatiotemporal variability. To assess the risk  
115 of liquefaction in the context of the freshwater-saltwater transition zone and during coastal inundation events, the vertical  
116 component of the hydraulic gradient is computed to evaluate the potential for liquefaction (as will be derived in the following  
117 section) with the application of the variable-head boundary condition and the inclusion of variable-density flow solutions. It  
118 should be highlighted that in the current work, no effects of long-term loading and residual liquefaction were investigated.  
119 Hereinafter, the vertical hydraulic gradients will be discussed rather than the pore pressures or heads. In the next section the  
120 equations for soil failure potential in terms of the head gradients are derived based on previous derivations (Briaud, 2013). The  
121 magnitude of the hydraulic head gradient (Figure 2), which according to Darcy's law is the magnitude of the seepage vector  
122 divided by the hydraulic conductivity, is denoted  $i$ . Other variables used in the following calculations are shown in Figure 2  
123 and summarized in Table 1.



124

125 Figure 2: A typical coastal hydrogeological system. Regional fresh (light blue) groundwater flows to the sea and upward due to  
 126 variable-density flow along the freshwater-saltwater (red) interface. In the nearshore area, focused groundwater discharge occurs  
 127 either into the sea (blue) or along a seepage face onshore. As shown in the top of the figure, when the surge begins, the direction of  
 128 flow reverses (infiltration), and when the sea level reaches its maximal level ( $h_{max}$ ) the surge retreats and the direction reverts back  
 129 (exfiltration). The upward (positive vertical component) of flow reaches a maximum when the sea level is back to pre-surge level,  
 130 before decaying to the steady-state magnitude.

131

132

133

134

135

136

137

138

139

140





141 **Table 1: Variables used in the theoretical calculations and numerical simulations.**

Parameter	Symbol	Value	Unit	Source
Hydraulic conductivity	K	10-100	m/d	Freeze & Cherry (1979)
Anisotropy	$K_x/K_z$	10		
Seawater density	$\rho_{sw}$	1025	Kg/m <sup>3</sup>	
Freshwater density	$\rho_{fw}$	1000	Kg/m <sup>3</sup>	
Local water density	$\rho_w$	1000- 1025	Kg/m <sup>3</sup>	
Solid material density	$\rho_s$	2650	Kg/m <sup>3</sup>	
Freshwater influx	$q_0$	0.01-0.04	m/d	
Aquifer storativity	$S_s$	$10^{-4}$	1/m	Freeze & Cherry (1979)
Porosity	$n$	0.3		
Longitudinal/Transverse Dispersivity	$\alpha_L/\alpha_T$	1/0.1	m	Gelhar et al. (1992)
Maximum surge height	$h_{0max}$	3	m	Chini & Stansby (2012)

142

### 143 3.1 The criterion for liquefaction under groundwater seepage

144 Some publications distinguish between the terms “liquefaction” and “quick sand”, with the former being used for earthquake-  
 145 induced fluidization of the soil, and the latter being related to failure due to upward flow (Briaud, 2013). However, the physical  
 146 meaning of the two is the same – geomaterial becoming weightless, which can result in erosion and sediment mobilization, or  
 147 loss of support of any infrastructure built into the soil. Here, the term liquefaction is used, although the analysis refers to surge-  
 148 induced changes in the subsurface flow rather than seismically induced flows. Following Briaud (2013), sand liquefaction  
 149 occurs when the pore pressure ( $u_w$ ) at a certain depth ( $z$ ) exceeds the total stress ( $\sigma$ ), i.e. when the effective stress ( $\sigma'$ ) goes to  
 150 zero:

$$\sigma' = \sigma - u_w \leq 0 \quad (1)$$

151 Neglecting the possibility that gas is still trapped in the pores and assuming a submerged unit weight can be applied, the  
 152 criterion for localized, momentary liquefaction in inundated regions can be written in a gradient form (Goren et al., 2013), in  
 153 which the vertical pore pressure gradient (positive downward gradient generates upwards flow) exceeds the submerged unit  
 154 weight of the soil ( $\gamma_{sub}$ ):



$$\gamma_{sub} + \frac{\partial u_w}{\partial z} \leq 0 \quad (2)$$

155 where

$$\gamma_{sub} = (1 - n) \cdot (\rho_s - \rho_{fw}) \cdot g \quad (3)$$

156

157 in which  $\rho_s$  is the density of the beach material (sand), and  $\rho_w$  is the density of the local water, which has a value between that  
158 of seawater ( $\rho_{sw} \approx 1025 \text{ kg/m}^3$ ) and freshwater ( $\rho_{fw} \approx 1000 \text{ kg/m}^3$ ). This failure criterion is similar to Yeh and Mason  
159 (2014), who studied liquefaction of a fully saturated sediment following a tsunami.

160 The constant value of porosity ( $n=0.3$ ) is typical for sandy soils, but neglects localized variations in sand bulk density in the  
161 simulated area. Furthermore, it is noted that the use of the submerged unit weight of soil is likely an underestimate of the actual  
162 unit weight for soils under storm-surge conditions, since saturated conditions may prevail prior to inundation and the saturated  
163 unit weight is higher than the submerged ( $\gamma_{sub} = \gamma_{sat} - \gamma_{fw}$ ). However, this work aims to harness a hydrologic modeling  
164 framework to assess the spatio-temporal distribution of surge-induced changes in hydraulic gradients. To that end, the  
165 liquefaction assessment is limited to the effects of vertical pressure gradients, momentary liquefaction, and the application of  
166 the submerged unit weight. It should be noted that studies have shown partially saturated sediments (e.g., in inundation areas)  
167 are typically prone to momentary liquefaction (Mory et al., 2007; Yeh and Mason, 2014). Mory et al. (2007) showed that even  
168 a 6% air content may alter the potential for momentary liquefaction. For the gradient-form criterion to hold, this condition  
169 would need to be met continuously from the surface to the depth of the liquefied layer (Goren et al. 2013), as accounted for in  
170 the analysis below.

171 Here, the momentary liquefaction criterion is related to vertical components of seepage vectors to compare the results of the  
172 groundwater model with the failure criterion. The 3D model considered here (see below) could be used to examine the  
173 horizontal components too, and to analyze the potential for shear failure, not only for momentary liquefaction (Zen et al.,  
174 1998). However, for the sake of simplicity and in the interest of focusing on the questions addressed here, such an expansion  
175 is not attempted in the current study. It would require further assumptions on the soil characteristics (internal friction, cohesion)  
176 and a localized analysis of the local slopes for each point in the domain. According to Darcy's law the vertical flow velocities  
177 ( $v_z$ ) are equal to the product of the (local) vertical head gradient and the vertical hydraulic conductivity  $K_z$ :

$$v_z = -K_z \left( \frac{1}{\rho_{fw}g} \frac{\partial u_w}{\partial z} + 1 \right) \quad (4)$$

178

179 thus, the vertical pressure gradient becomes

$$\frac{\partial u_w}{\partial z} = -\rho_{fw}g \left( \frac{v_z}{K_z} + 1 \right) \quad (5)$$

180





181 Substituting Equations 3 and 5 into Equation 2 yields:

$$(1 - n) \cdot (\rho_s - \rho_{fw}) \cdot g - \rho_{fw} g \left( \frac{v_z}{K_z} + 1 \right) \leq 0 \quad (6)$$

182

183 From Equation 6, the value of the critical vertical head gradient ( $i_c$ ) is that above which the effective stress is zero or less:

$$\left( \frac{v_z}{K_z} \right)_c \equiv i_c = (1 - n) \cdot \frac{\rho_s - \rho_{fw}}{\rho_{fw}} - 1 \quad (7)$$

184 This result is similar to that derived by Briaud (2013), but here it is derived for saturated groundwater flow, which is the  
185 appropriate formulation for the scenario of surge-induced changes in the groundwater flow regime. Using Darcy's law in this  
186 context assumes that during the surge the groundwater flow remains largely laminar, which is likely for storm-surge conditions  
187 and is a common assumption in similar studies (Abdollahi & Mason, 2020; Guimond & Michael, 2021; Paldor & Michael,  
188 2021; Yang et al., 2013; Yu et al., 2016). For convenience, the magnitude of negative (destabilizing) vertical head gradients  
189 which initiate positive vertical velocities, is hereinafter denoted  $i_z$  and presented in positive values. Using typical values for  
190 porosity, solid particle density, and freshwater density for beach material ( $n = 0.3$ ;  $\rho_s = 2650 \text{ kg/m}^3$ ;  $\rho_{fw} =$   
191  $1000 \text{ kg/m}^3$ , respectively), Equation 7 suggests the critical value of vertical head gradient is about  $i_c = 0.15$ . The following  
192 analyses use this value as a threshold for liquefaction, with simulated values of  $i_z$  normalized by the critical value  $i_c = 0.15$   
193 as the seepage-liquefaction factor (SLF):

$$SLF = \frac{i_z}{i_c} \quad (8)$$

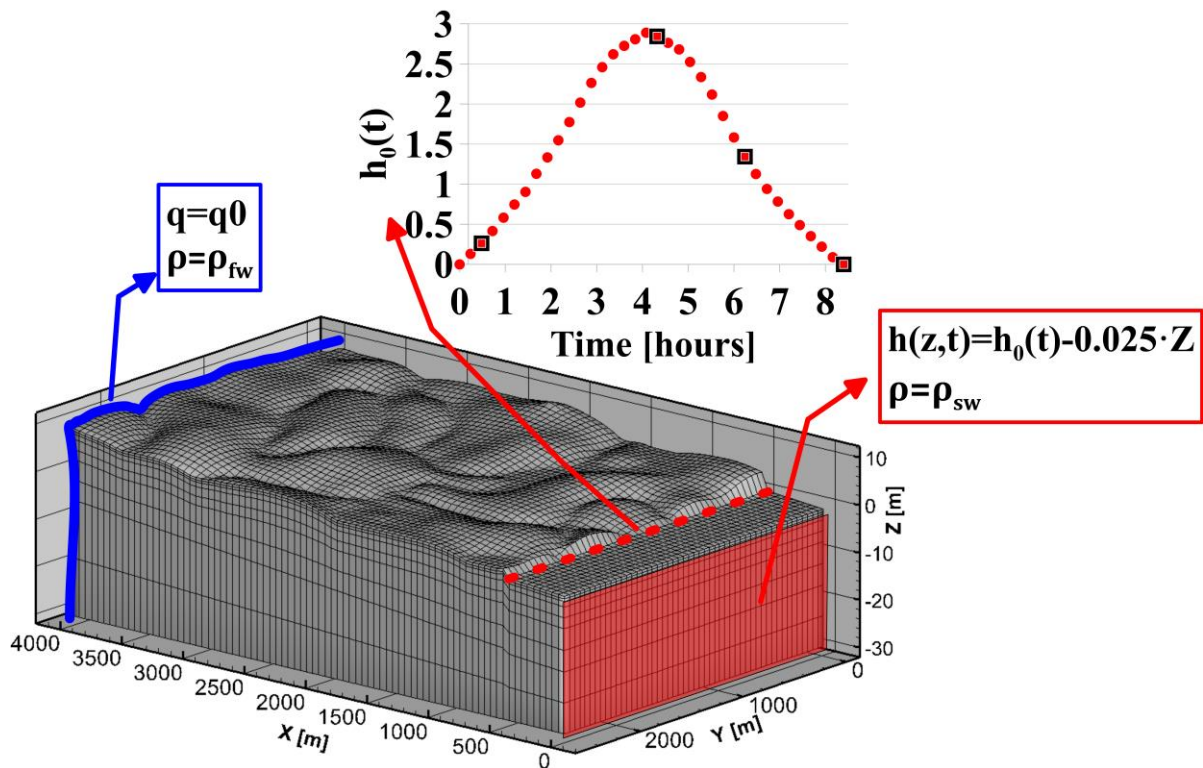
194 In Equation 8,  $i_z$  is the actual simulated or observed vertical head gradient, defined as  $i_z = -\frac{v_z}{K_z}$  (Eq. 4) and  $i_c$  is the theoretical  
195 liquefaction threshold (Eq. 7). Thus, any point in space and time in which simulated SLF is close to 1 is potentially nearing  
196 liquefaction. A layer in which SLF approaches 1 continuously from the surface to a depth  $Z_l$  is considered a "critical layer" of  
197 thickness  $Z_l$ .

#### 198 4 Hydrologic model

199 The effect of storm surges on groundwater flow is simulated using Hydrogeosphere (HGS) – a 3D numerical code that couples  
200 surface and subsurface flow and solute transport (Therrien et al., 2010). For the surface flow, HGS solves the Saint-Venant  
201 equations (also known as nonlinear shallow water equations), and for the variably saturated subsurface flow it solves the  
202 Richards equation. The salt transport equation is solved in its advective-dispersive form, and the variable-density flow solution  
203 is coupled to the transport solution through a linear equation of state. Hydrogeosphere has been successfully employed to  
204 simulate storm surges in several recent studies (Guimond & Michael, 2020; Yang et al., 2013, 2018; Yu et al., 2016), and here  
205 it is applied to assess the risk for sediment liquefaction and erosion from surge-induced pore water head gradients. This is a  
206 novel interdisciplinary approach, applying a robust 3D hydrologic model in the context of coastal geomechanics.



207 The model domain (Figure 3) is 4000 m (cross-shore, X) by 2500 m (alongshore, Y), extending to a depth of 30 m below the  
208 mean sea level ( $Z=0$ ). The terrestrial extent of the domain is 3550 m ( $450 < X \leq 4000$ ), with the ocean spanning  $0 \leq X \leq 450$  (Figure  
209 3). The elevation at the ocean side boundary is  $Z(X=0)=-1$ , so the seafloor slope is  $1/450 \approx 0.0022$ . This slope is representative  
210 of U.S. Atlantic and Gulf coastal systems averaged over large cross-shore distances (e.g., from the beach to the mid continental  
211 shelf). Although local slopes in the surf and beach often are much steeper than those used here, this study is focused on the  
212 liquefaction in and near the inundated dune system. The average surface elevation inland ( $X=4000$  m) is 5 m, so that the  
213 average land surface slope is  $5/3550 \approx 0.0014$ . Thus, there is a change in average slope at the coastline, as the offshore portion  
214 is steeper ( $\sim 0.0022$ ) than the onshore (0.0014), as in many coastal areas. A simulation with a -0.5 m sea level (i.e., still water  
215 shoreline at  $X=225$  m) indicates that critical vertical hydraulic gradients occur near this change in overall slope irrespective of  
216 the shoreline location (Figure A1 in the Appendices). A simulation with a larger beach slope ( $Z(X=0) = -6$ ; slope =  $6/450 = 0.0130$ )  
217 resulted in similar vertical hydraulic gradients as the baseline slope (0.0022) (Figure A2 in the  
218 Appendices), indicating that although the baseline slope is lower than typical, the analysis based on it is also valid for steeper  
219 slopes. The domain of the finite difference model consists of 44,000 rectangular cells, where the cell sizes in the X and Y  
220 direction are 25 and 50 m, respectively. The cell size in the Z direction varies from 8 m in the bottom of the domain to about  
221 0.5 m in the top 2 m to balance between computation time and the resolution necessary to resolve the dynamics close to the  
222 surface (Figure 3). The homogenous hydraulic conductivity  $K_x$  is 50 m/d for the baseline simulation and  $K_x$  varied between  
223 10 and 100 m/d in sensitivity analyses. In all simulations, the anisotropy was 10 (i.e., the vertical hydraulic conductivity,  $K_z$ ,  
224 was 10 times lower than the horizontal hydraulic conductivity,  $K_x$ ). This range of hydraulic conductivity with a porosity,  $n$ , of  
225 0.3 is typical for sandy beach environments (Freeze and Cherry, 1979). Although a change in  $K$  could be associated with a  
226 change in  $n$  for some sediments and mixtures, due to the potentially complex relationships between porosity and the sediment  
227 textural properties, including grain size distributions, shapes, and  $K$ , the porosity was kept constant in the simulations presented  
228 here.



229

230 **Figure 3: Hydrogeosphere model domain as a function of the vertical  $Z$ , cross-shore  $X$ , and alongshore  $Y$  dimensions, boundary**  
 231 **conditions (red and blue boxes), and the surge height evolution curve (inset). The blue curve is the terrestrial freshwater recharge**  
 232 **boundary, the red rectangle is where a fixed seawater head and concentration are applied to the subsurface domain, and the red**  
 233 **dashed line is where the sea level height boundary condition ( $h_0(t)$ ) is applied on the surface domain. For the steady-state**  
 234 **simulations  $h_0(t)=0$ , and for the transient simulations the curve in the inset is applied. The black squares in the inset mark the**  
 235 **times plotted in Figure 5.**

236

237 The boundary conditions in the simulations were applied in two stages – a steady-state period and a transient surge period. For  
 238 the steady-state simulations, terrestrial boundary conditions of constant freshwater specific recharge ( $q=q_0, \rho=\rho_{fw}$ ) were  
 239 applied on the vertical wall at the inland edge of the subsurface domain at  $X=4000$  (blue curve in Figure 3) (Ataie-Ashtiani et  
 240 al., 2013; Yang et al., 2018; Yu et al., 2016). The opposite edge of the domain at  $X=0$  (red wall in Figure 3) was a typical sea  
 241 boundary condition with depth-dependent head and saline ocean water ( $h=-0.025 \cdot Z; \rho=\rho_{sw}$ ). On the surface domain the only  
 242 boundary condition is applied on the coastline  $X=450$  m, red dashed line in Figure 3) as a fixed, time-dependent head ( $h=h_0(t)$   
 243 ( $t$ ) and seawater density ( $\rho=\rho_{sw}$ ). The applied head on the coastline was held at zero through the steady-state simulations.  
 244 For the transient surge simulations, the coastline head was varied over 8.5 hours between zero and a 3 m maximum surge  
 245 height (inset in Figure 3). A sea level of 3 m above the mean represents a combined high-tide and surge event with a projected

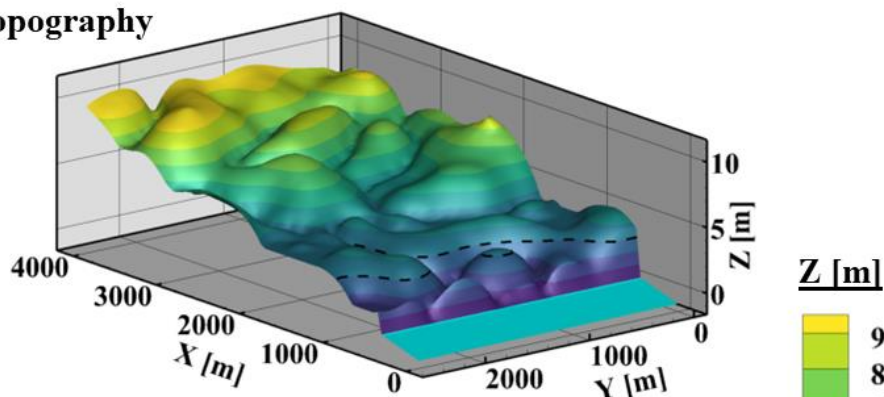


246 return period of 100 yr by the year 2050 in the East Coast of the United States (Tebaldi et al., 2012). The ocean surface was  
247 assumed to be spatially constant at any time, and effects of wind waves were not simulated.

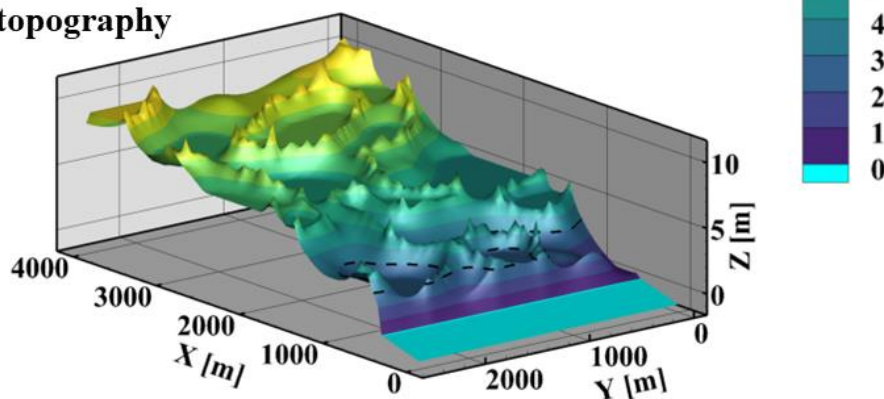
248 The sensitivity of the results to the topography and hydrogeologic parameters was tested, including freshwater influx ( $0.01 <$   
249  $q_0 < 0.04$  m/d, Figure 3 and Table 1) and hydraulic conductivity ( $10 < K_x < 100$  m/d, Table 1, typical values for sandy  
250 beaches (Freeze & Cherry, 1979)). For the baseline hydraulic conductivity ( $K_x=50$  m/d) the range of overall (land-to-sea)  
251 hydraulic gradients, calculated as  $q_0/K_x$ , was 0.0002 and 0.0008, on the lower side of typical coastal settings (roughly  
252 around 0.0010), and so the calculated hydraulic gradients in the current analysis are considered a conservative estimate. Two  
253 topographies (Figure 4) (Yu et al., 2016) were generated with ARCMAP 10.0 Geographic Information System (GIS) software  
254 (ESRI, 2011), using multigaussian random fields that were transformed (Zinn & Harvey, 2003) to connect either topographic  
255 highs or lows rather than the median topographic values as in the non-transformed multigaussian fields. The first topography,  
256 named “River” (Figure 4a), is characterized by surface depressions that connect to the sea. The topographic lows are connected,  
257 forming “river”-like patterns in the surface morphology), superimposed on the background slope of 0.0014. The second  
258 topography, “Crater” (Figure 4b), features connected crests surrounding disconnected surface depressions, such that the highs  
259 are connected, forming “crater” like shapes. The two topographies do not mirror each other (Figure 4), but represent reverse  
260 alongshore trends near the shoreline ( $450 < X < 500$  m) in which the area around  $0 < Y < 300$  m ( $2200 < Y < 2500$  m) is the highest  
261 (lowest) for the River topography and lowest (highest) for the Crater topography. Comparisons with real topographies of the  
262 Delaware coastal plains (Yu et al. 2016) suggested that the River topography best represents real-world meso-topography.  
263 However, the Crater topography provides important insights to how meso-topography controls the evolution of head gradients  
264 during storm surges. In extreme flooding events (e.g., tsunami), large-scale changes in surface morphology (e.g., landslides)  
265 may alter the pore-pressure distribution. These effects were excluded from the current work, as the simulated surface was  
266 considered constant throughout the simulation. Additionally, soil deformation and the resultant stress re-distribution were not  
267 considered in this model, as the hydrologic model (HGS) assumes constant porosity.



### a. River topography



### b. Crater topography



268

269 **Figure 4: (a) River and (b) Crater topographies as a function of the vertical Z, cross-shore X, and alongshore Y coordinates. Light**  
270 **blue is the offshore bathymetry, and the coastline is at X=450 m. The overall slope accounting for macro-topography is the same for**  
271 **both topographies, the average elevation at X=4000 m is ~5 m, making it a slope of  $5/3550 \approx 0.0014$ . The dashed black curve marks**  
272 **the Z=3 m contour, which is equal to the maximum surge-induced sea level ( $h_{max}$ ).**

273

274

275 For each simulation, the vertical hydraulic gradients ( $i_z$  in Equation 8) are calculated over a vertical slice along the coastline,  
276 i.e., the plane defined by X=450, and normalized by the threshold defined by Equation 7 ( $i_c$ ) to calculate the SLF (Equation  
277 8). As explained in Section 3 above, values of SLF that approach 1 are considered critical for liquefaction. When  $SLF \ll 1$  the  
278 simulated surface theoretically is stable. Only upward, destabilizing velocities (exfiltration) are considered, and so negative  
279 velocities were assigned a value of  $i_z=0$ .

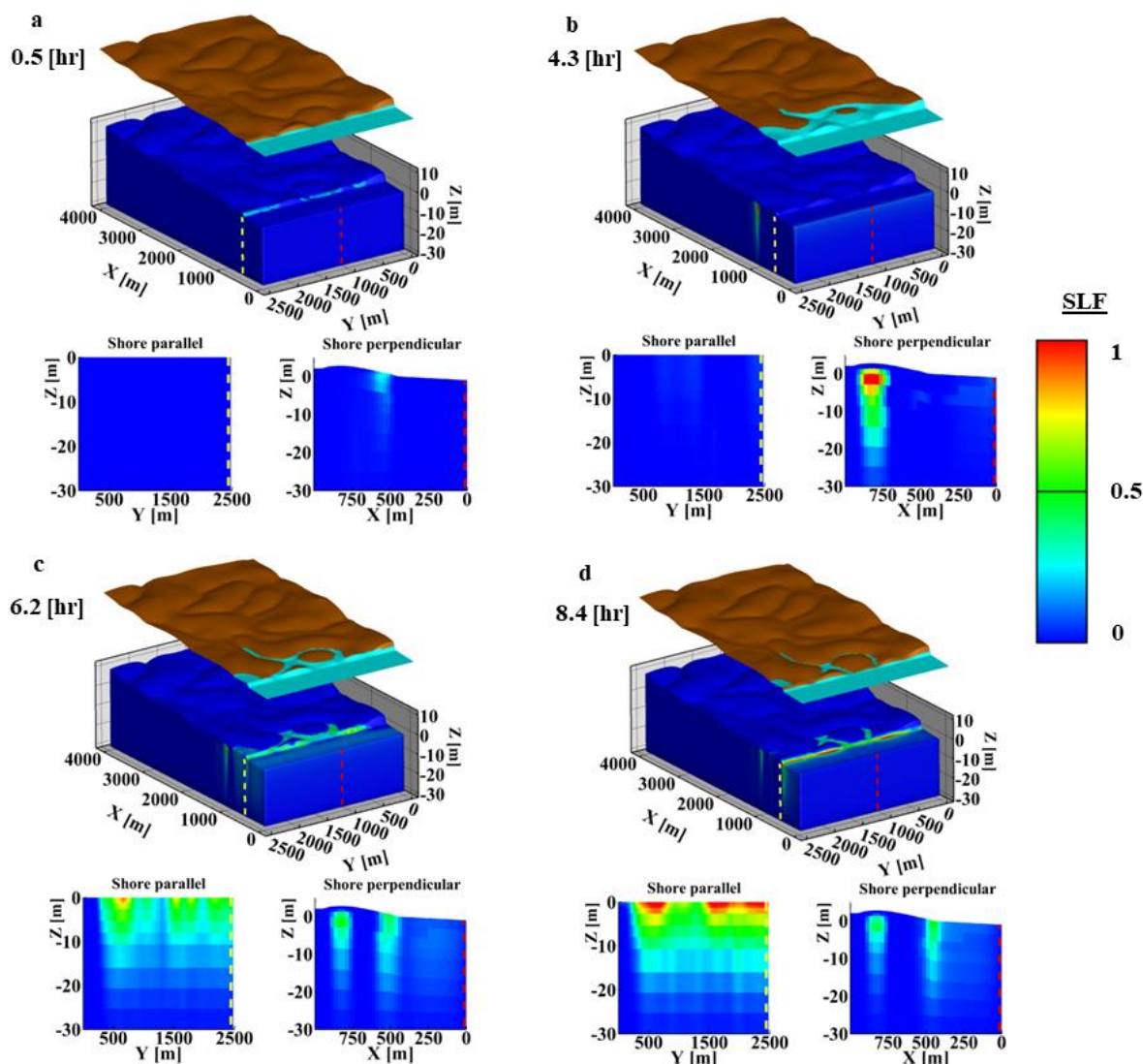
280



## 281 **5 Results**

282 The baseline case ('River' topography with  $q_0=0.02$  m/d ;  $K_z=5$  m/d) includes a 3 m surge and simulates the resultant  
283 changes in head gradients (Figure 5). During the inundation stage when sea level is increasing, the head gradients increase  
284 landward in front of the moving surge, and in the flooded zone there is infiltration (head decreases downward,  $\nabla h > 0$ ). After  
285 the peak of the inundation, when the high-water levels begin to recede, downward gradients (i.e., head increases downward,  
286 potentially destabilizing) develop underneath the still-water shoreline ( $X=450$  m). These downward gradients increase in  
287 magnitude as the water level recedes, and the subsurface system relaxes back to background levels (not shown in Figure 5)  
288 within ~50 days for the high-K aquifers to ~500 days for the low-K aquifers, similar to prior simulations of storm impacts  
289 (Robinson et al. 2014). The peak alongshore variation of the vertical hydraulic gradients occurs at the end of the inundation  
290 ( $t=8.4$  hr, Figure 5d). The vertical hydraulic gradients onshore of the inundation front during run-up (Figure 5b) develop in  
291 subaerial areas, and therefore the calculated SLF for these zones is based on the saturated unit weight ( $\gamma_{sat}=\gamma_{sub}+\gamma_{fw}$ ) of  
292 sediments rather than the submerged unit weight ( $\gamma_{sub}$ , Equation 3), and the model-predicted liquefaction may not occur in  
293 real systems because saturated soils are more stable than submerged ones (Briaud, 2013).





294

295 **Figure 5: Surface inundation and vertical hydraulic gradients at (a) 0.5, (b) 4.3, (c) 6.2, and (d) 8.4 hr after the simulated surge**  
 296 **begins (for the surge height at these times refer to Figure 3). In each panel, the surface domain is shown on top, the subsurface 3D**  
 297 **domain and vertical gradients are shown below, and two cross sections through the subsurface are shown: shore-parallel (left in**  
 298 **each panel) and shore-perpendicular (right). The locations of the sections are shown on the 3D plot as red dashed lines (for shore**  
 299 **perpendicular) and yellow dashed lines (for shore parallel). The upper two panels are during the run-up stage and the lower are**  
 300 **during the retreat stage. Refer to Figure 3 for the surge height at each time shown here. Note that downward gradients (head**  
 301 **increases downward) are plotted as positive and upward gradients (head increases upward) are plotted as zero.**

302

303 The head changes ( $\Delta h$  in Figure 6) between the steady state and the peak of the inundation inversely follow the topography  
 304 (black contours in Figure 6a and b). For the highest topographic elements ( $Y=0$  m for the “River” and  $Y=2500$  m for the

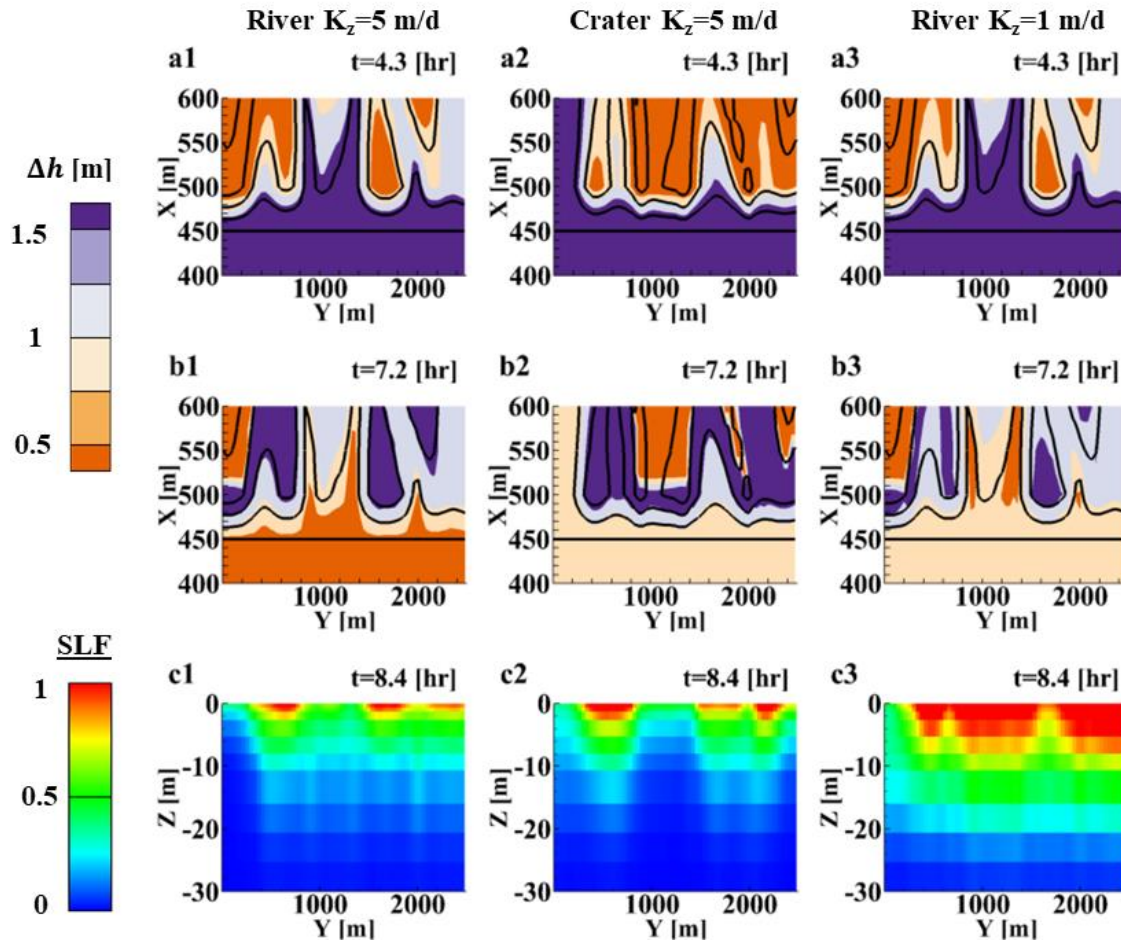




305 “Crater”), which are not inundated, the simulated heads are approximately equal to the maximum ocean level at the dune crest  
306 ( $X \sim 460$  m), and decay inland over  $\sim 100$  m, roughly consistent with field observations (Figure 1). The maximum head changes  
307 (purple colors in Figure 6a) inland of the shoreline ( $X > 475$  m) at peak surge occur in the inundated topographic lows. Toward  
308 the end of the simulated surge ( $t = 7.2$  hr, Figure 6b) the surge-induced overpressures are released in the topographic lows (low  
309 values of  $\Delta h$  in Figures 6b). The head differences also are low in the topographic highs because the heads there did not rise  
310 significantly during inundation. In contrast, the intermediate topographic features show high head differences (dark purple in  
311 Figure 6b). The lowest near-shore ( $450 \leq X \leq 500$  m,  $900 \leq Y \leq 1200$  m) topography undergoes similar head changes during the  
312 peak surge for high and low  $K$  (compare Figure 6a1 with 6a3). However, in the low  $K$  case (Figure 6a3, 6b3), the heads are  
313 not released effectively as the surge recedes, and significant excess heads of  $\sim 1$  m difference remain near the end of the surge  
314 (compare Figure 6b3 with 6b1 for  $X \sim 450$  m).

315 When the surge has retreated ( $t = 8.4$  hr), the head gradients at the dune toe (initial shoreline) ( $X = 450$  m) reach their maximum  
316 (Figure 6c1-c3). In all simulations critical gradients ( $SLF \rightarrow 1$ , red zones in Figure 6 c1-c3) are simulated at some locations  
317 below the shoreline, supporting the findings of several recent field studies in which momentary liquefaction was observed in  
318 response to inundation events (Sous et al., 2016; Yeh & Mason, 2014). The alongshore distribution of the surge-induced  
319 gradients is insensitive to the freshwater influx ( $q_0$ ), even though the antecedent local hydraulic gradients differed by up to a  
320 factor of 4 between simulations (Figure A3 in the Appendices, note that the values of the antecedent local gradients are about  
321 an order of magnitude lower than the peak gradients). The depth and alongshore locations of the areas prone to liquefaction  
322 (i.e.,  $SLF \sim 1$ ) are sensitive to the topography (compare Figures 6 a1,b1,c1 with a2, b2, and c2) and the hydraulic conductivity  
323 (compare Figures 6 a1,b1,c1 with a3, b3, and c3). The two topographies exhibit a similar spatial pattern of SLF (Figure 6c1  
324 and c2) even though the differences in topography (Figure 4) cause significant differences in the surge-induced head changes  
325 (Figure 6 a1 and a2). For example, the area to the left of the domain ( $Y \leq \sim 300$  m) is a topographic low in the Crater topography  
326 and undergoes significant head changes at the peak of the inundation (Figure 6a2), whereas for the River topography there is  
327 a topographic high for  $Y \leq \sim 300$  m, which is not as strongly affected by the surge (Figure 6a1). However, in both cases this area  
328 is where the least significant vertical head gradients develop (Figure 6c1 and c2).

329 The hydraulic conductivity has a significant effect on the simulated surge-induced gradients (Figure A4 in the Appendices).  
330 Decreased hydraulic conductivity causes higher peak vertical gradients and changes the spatial (shore-parallel) distribution of  
331 the gradients (compare Figure 6c3 with 6c1, especially near  $Y = 1000$  m, and also see Figure A4). Furthermore, decreasing  
332 hydraulic conductivity alters the depth  $Z_1$  of “critical layers” with  $SLF = 1$  (Equation 8) (compare Figure 6c3 with 6c1). In  
333 the high- $K$  simulations (Figure 6c1 and c2), the depth  $Z_1$  of these “critical layers” with  $SLF \sim 1$  ranges between 0 and 2.5 m,  
334 and in the low- $K$  simulation (Figure 6c3)  $Z_1$  is up to  $\sim 5$  m.

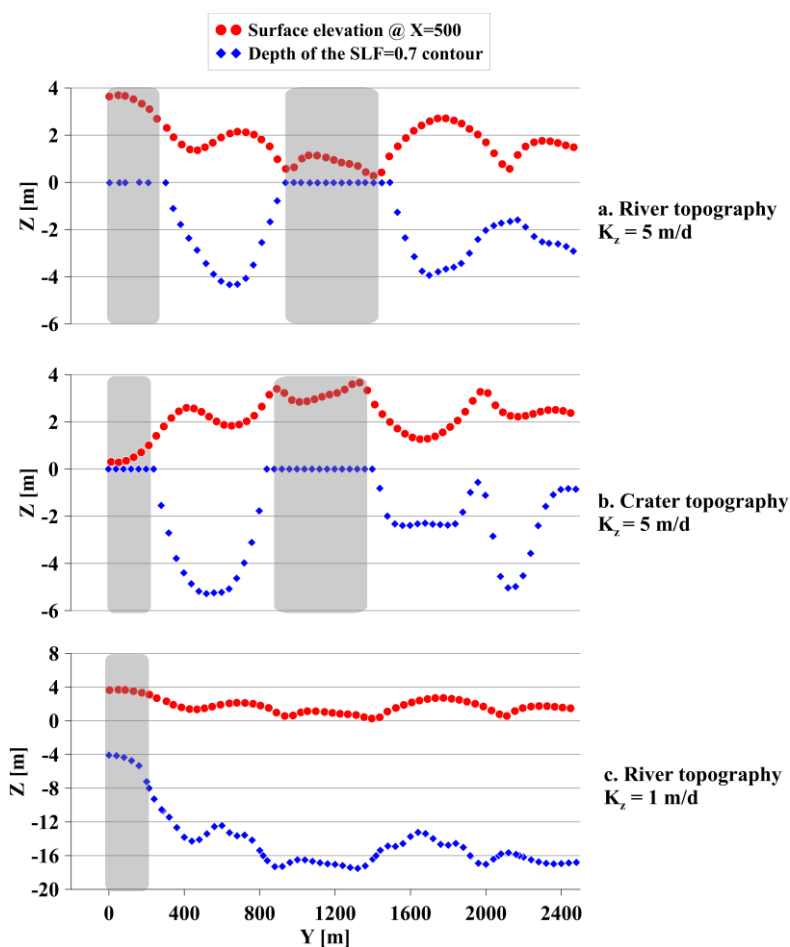


335  
 336 **Figure 6:** Top row (a1-a3): maps of the maximum near-surface head differences between those at the peak of the inundation and the  
 337 initial, pre-surge values (denoted  $\Delta h_1$ ) as a function of the cross-shore  $X$  and alongshore  $Y$  coordinate. Middle (b1-b3): maps of  
 338 the maximum subsurface head differences between those near the end of the surge ( $t = 7.2$  hr, Figure 3) and the initial, pre-surge  
 339 heads (denoted  $\Delta h_2$ ) as a function of  $X$  and  $Y$ . Bottom (c1-c3): Liquefaction potential SLF at the shoreline,  $X = 450$  m, as a function  
 340 of the vertical  $Z$  and alongshore  $Y$  coordinate. These 3 metrics are plotted for River topography with  $K_z=5$  m/d (left, a1-a3), Crater  
 341 topography with  $K_z=5$  m/d (center, a2-c2) and River topography with  $K_z=1$  m/d (right, a3-c3). In the upper and middle panels (map  
 342 views a1-a3 and b1-b3) the black contours are surface elevation with 1 m intervals. The horizontal line at  $X=450$  is the coastline  
 343 ( $Z=0$ ). The lower panels are plotted for  $t=8.4$  hr, the time at which the vertical gradients peaked in all simulations all along the  
 344 coastline.

345  
 346 The relationship between coastal topography and the surge-induced liquefaction potential is evident when comparing the  
 347 surface elevations 50 m landward of the coastline ( $X=500$  m) and the peak vertical gradients below the coastline for different  
 348 topographies and  $K$ 's (Figure 7). Here, the  $SLF=0.7$  contour is used for statistical stability (there are more locations with  
 349  $SLF \geq 0.7$  than with  $SLF=1$ ). For both topographies, when  $K$  is high,  $SLF$  typically remains less than 0.7 (in Figure 7 where the



350 blue diamonds = 0) at the shoreline adjacent to the highest ( $Z > 3\text{m}$ ) and lowest ( $Z < 1\text{ m}$ ) topographic elements (marked by  
 351 gray rectangles in Figures 7a and b), suggesting the intermediate topographic features may lead to the strongest vertical  
 352 hydraulic gradients and liquefaction potential. However, the height of intermediate features that produce high gradients may  
 353 be dependent on the site and hydrogeological parameters. For example, in the two simulations with higher  $K_z$ , 1-3 m  
 354 topographic features are associated with most of the significant surge-induced gradients (Figure 7a and b). For the lower  $K_z$   
 355 case, significant gradients occur also below the lowest area (Figure 7c), and only the highest area that is not inundated does  
 356 not develop significant gradients (gray rectangle in Figure 7c).



357  
 358 **Figure 7: Topographic elevation at  $X=500\text{ m}$  (50 m onshore of the shoreline, red circles) and depth of the SLF=0.7 contour below**  
 359 **the shoreline (blue diamonds) versus alongshore coordinate  $Y$  for (a) the River topography with  $K_z=5\text{ m/d}$ , (b) Crater topography**  
 360 **with  $K_z=5\text{ m/d}$ , and (c) River topography with  $K_z=1\text{ m/d}$ . Deeper locations of the SLF=0.7 contour (blue diamonds) mean thicker**  
 361 **“critical layers”. The places where no significant critical layer develops (i.e., the elevation of the SLF=0.7 contour is  $Z=0$ ) are marked**  
 362 **by gray rectangles.**



## 363 **6 Discussion**

### 364 **6.1 Alongshore variability**

365 The simulations suggest that alongshore variability of the magnitudes of the vertical gradients is strongly associated with the  
366 coastal topography (Figures 5-7). To induce high gradients and deep critical layers when pressures are released, it is necessary  
367 to have inundation resulting in high infiltration and increased heads. Thus, topographic highs that are not inundated cannot  
368 develop high gradients (Figures 6 and 7). Meanwhile, overpressures often are released efficiently from inundated areas as the  
369 surge recedes. Topographic elements that are low enough to be inundated, but are also high enough to limit the post-surge  
370 exfiltration may prevent release of pressures, possibly explaining the correlation of liquefaction potential with intermediate  
371 topographic features (1-3 m high for a 3 m surge). This explanation would suggest that the characteristic elevation of  
372 “intermediate features” would scale with the surge magnitude. Pressure releases also can be limited by low hydraulic  
373 conductivity. Thus, the simulations suggest the areas most susceptible to destabilization (i.e., deep critical layers) are those  
374 where topography is low enough to be inundated widely, and high enough that the pressure release is limited. The range of  
375 susceptible topographic elements depends on hydraulic conductivity, which also has a sweet spot of vulnerability: A simulation  
376 with even lower hydraulic conductivity ( $K_z=0.05$ ) showed that very low values of  $K$  limit the surge-induced infiltration and  
377 thus critical gradients develop only to a limited vertical extent and the alongshore variability (i.e., the dependency on onshore  
378 topography) diminishes (Figure A5 in the Appendices).

### 379 **6.2 Cross-shore spatiotemporal variability**

380 During the flooding stage, negative vertical gradients (infiltration) that do not promote sediment instability occur at and  
381 seaward of the moving inundation front. Positive vertical gradients occur landward of the front (top right panel in Figure 5)  
382 owing to alteration of the pre-existing steady-state flow field (Figure 2) by the advancing overpressures from the surge.  
383 However, the simulated values of  $SLF=1$  inland of the inundation front are not necessarily sufficient to liquefy the surface,  
384 because the actual weight of the unsubmerged soil is greater than  $\gamma_{sub}$  (Equation 2). Nevertheless, the liquefaction potential  
385 calculated here may still represent an underestimate, as Mory et al. (2007) showed that as little as 6% air content in the pores  
386 may reduce the required pressure difference to liquefy the sediment by 0.01 m. This highlights the need to consider air contents  
387 in future studies. Furthermore, these inland processes, and the potential for liquefaction in these areas, may be affected by  
388 vegetation, trapping of gases, hysteresis of wetting and drying, and other processes that have not been considered here.  
389 Nevertheless, the presented approach demonstrates the feasibility and a pathway to implement the concept of surge-induced  
390 momentary liquefaction in a hydrological model that can predict variable-density groundwater flow in coastal and estuarine  
391 environments.

392 The receding water levels after the peak of the surge allow fast release of the elevated heads that developed in the inundated  
393 area, because the overlying burden of surge waters is removed abruptly. For all simulations at all alongshore locations, the  
394 positive head gradients simultaneously reached a maximum when the water had receded completely ( $t=8.4$  hr) and all the



395 inundation water overburden was released. The rate of head release determines the hydraulic gradients that occur in the soil  
396 material, so that faster release of the overpressures produces lower positive head gradients. As the water recedes, the highest  
397 release rates, and thus overpressures, develop under the beach area, where the slope changes from a terrestrial average slope  
398 of 0.0014 to the seafloor slope of  $\sim 0.0022$  (Figure 3). Thus, the simulations suggest the highest surge-induced gradients might  
399 be expected under convex topography, for example near the berm or near a scarp in the beach face.

### 400 **6.3 Implications for coastal engineering**

401 Most previous studies of extreme wave-induced pressurization in coastal environments focus on cross-shore variability (Sous  
402 et al., 2013, 2016; Turner et al., 2016; Yeh & Mason, 2014). Here, it is shown that under realistic hydrogeological conditions  
403 (surge height, topography, groundwater flow regime – all based on values that are commonly observed in natural systems)  
404 with alongshore varying topography there can be significant differences in storm-induced maximum hydraulic gradients and  
405 in the depths of corresponding critical layers over small distances along the coastline ( $<500$  m) (Figure 6). The simulations  
406 suggest that beach and dune morphology are important factors determining the spatial variability of high gradients. Although  
407 low-lying coastal areas may endure the greatest flooding, the largest hydraulic gradients and the deepest liquefaction layers  
408 may occur at the toes of the intermediate-scale (1-3 m high for a 3 m surge) topographic features. While discussing practical  
409 implications of the present analysis, it is important to remember that, as noted above, the model adopted here is a hydrological  
410 model that does not explicitly simulate the soil dynamics and the surface and subsurface domains were assumed constant with  
411 time through the simulations. This assumption overlooks other dynamic controls on the development of stresses, such as soil  
412 deformation and surface erosion. Moreover, the analysis presented here isolates the vertical seepage component to calculate  
413 the potential for momentary soil liquefaction. In a 3D framework, horizontal seepage components likely come into play and  
414 other failure mechanisms, such as shear failure, are likely too (Zen et al., 1998). However, for the conclusions drawn here  
415 regarding the spatio-temporal distributions of surge-induced gradients, the hydrologic modeling provides an important tool to  
416 study the hydrogeological aspect of the problem. The model could be further expanded to include other components in future  
417 work.

### 418 **7. Conclusions**

419 Field measurements from Duck, North Carolina, show that during Hurricane Joaquin the groundwater flow regime at the ocean  
420 side was impacted substantially, and the hydraulic head gradient reversed its direction, followed by a period of recovery during  
421 which downward gradients (upward fluxes) were regenerated. This suggests that hydraulic gradients generated by storm surges  
422 may substantially affect the stability of beach surfaces. We explored this idea and its generality by harnessing a robust  
423 hydrological model to simulate a generalized coastal system and found that in the nearshore area, surge-induced hydraulic  
424 gradients may peak to critical levels that could potentially induce sand liquefaction. The locations where these critical gradients  
425 occur are transient and depend on the beach morphology and hydraulic conductivity. Both the elevation of topographic features

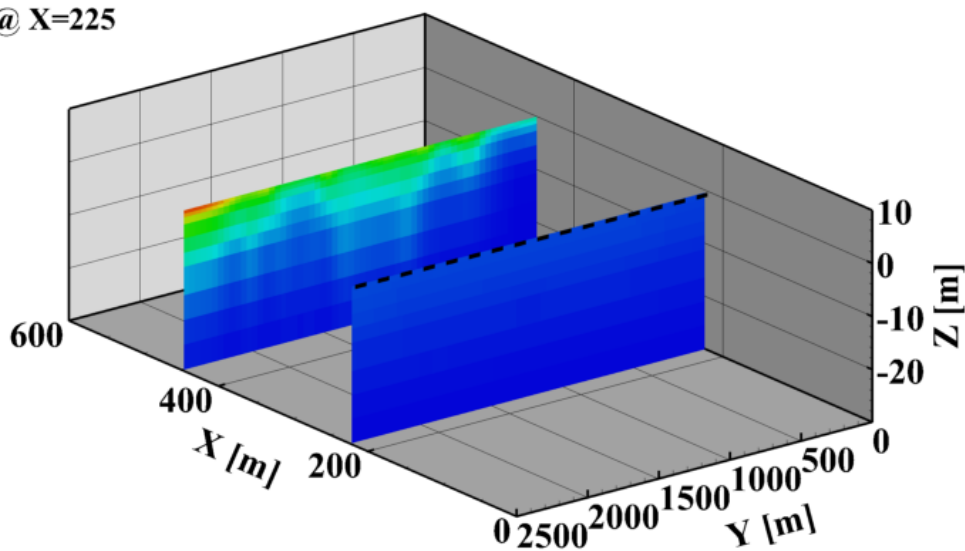


426 and their permeability are important factors in promoting liquefaction. Elevations must be low enough to become inundated,  
427 and high enough to retain elevated heads needed to build critical gradients. Similarly, hydraulic conductivity must be high  
428 enough to allow floodwater to infiltrate, but low enough that water is not drained immediately such that critical gradients can  
429 persist. This alongshore variability has not been observed in field measurements because the common approach in field studies  
430 is to measure the cross-shore variability of hydraulic heads during storms. Importantly, this work presents a novel approach to  
431 bridge the gap between coastal hydrology and coastal engineering, incorporating robust hydrogeological modeling in a  
432 geotechnical framework.

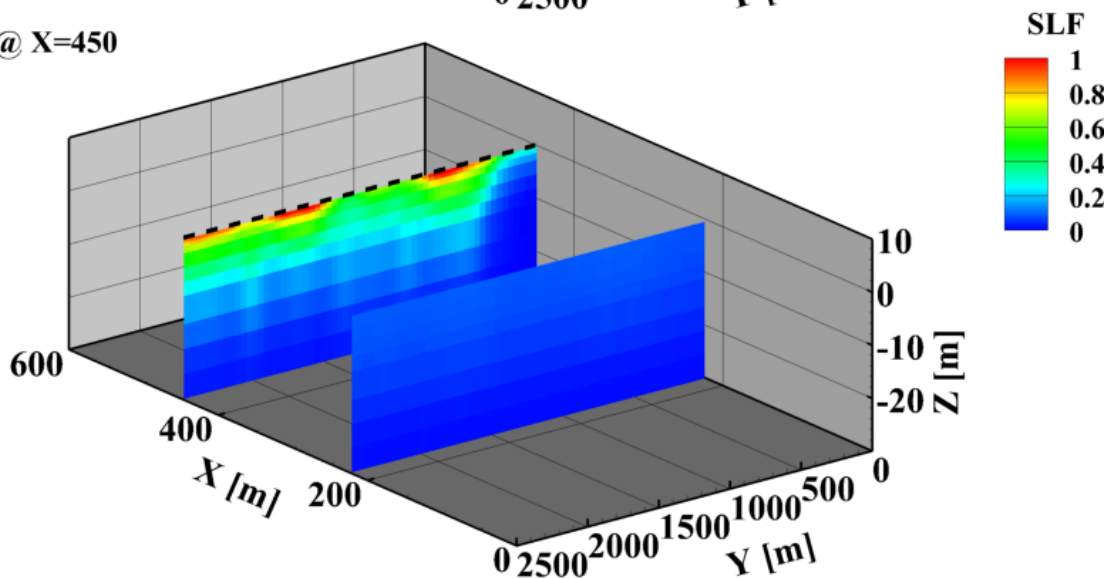


433 8. Appendices

a. Coastline @  $X=225$



b. Coastline @  $X=450$

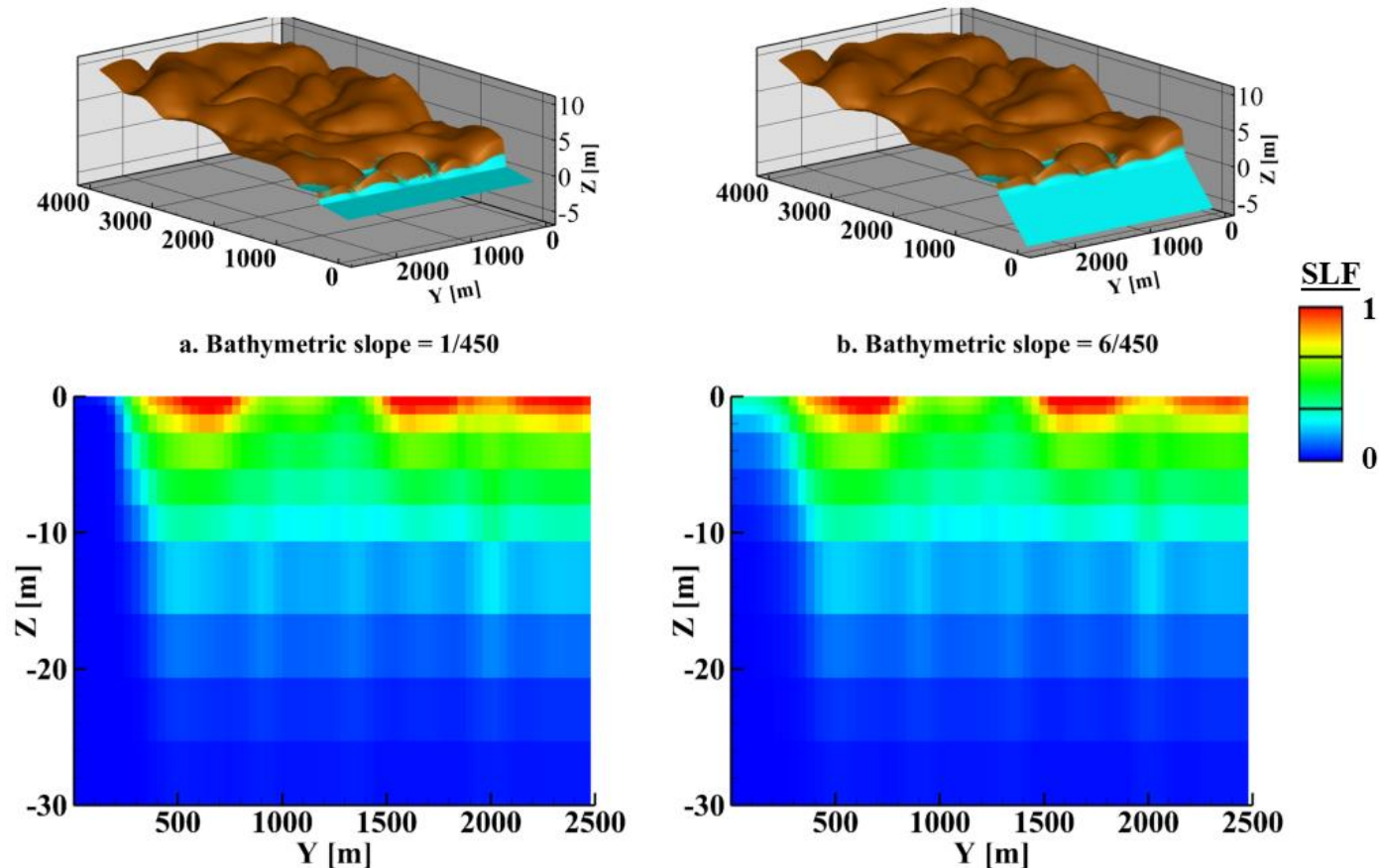


434

435 **Figure A1: Contours (color scale on the right) of peak SLF ( $t=8.4$  hr) as a function of the vertical Z, cross-shore X, and**  
436 **alongshore Y coordinate for (a) a simulation with the coastline at  $-0.5$  m ( $X = 225$  m) and (b) a simulation with the**  
437 **coastline at  $0$  m ( $X = 450$  m). The dashed black lines mark the coastline in each respective simulation. The slice with**  
438 **high SLF values in (a) is not underneath the simulated coastline.**

439





440

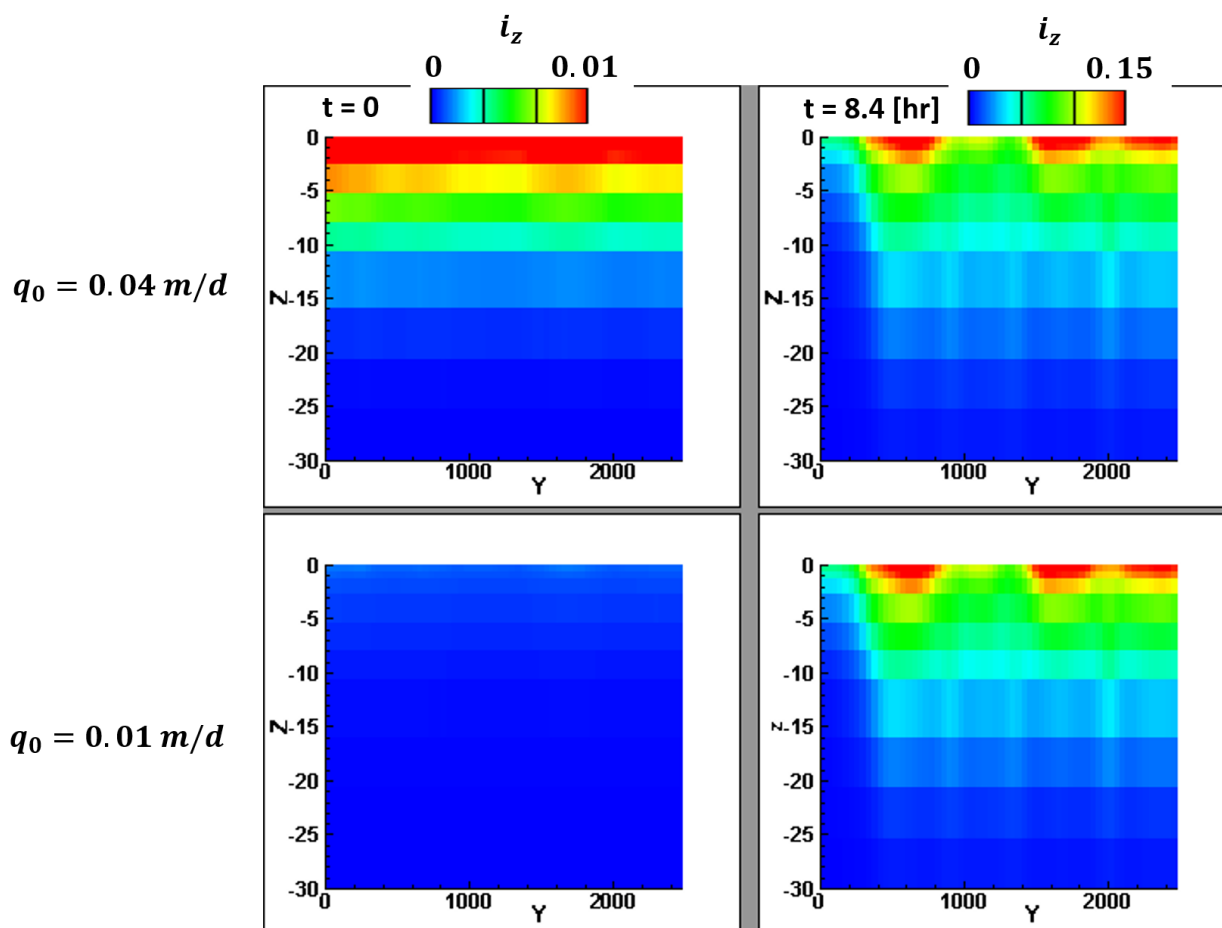
441 **Figure A2: Contours (color scale on the right) of peak SLF ( $t = 8.4$  hr) for a simulation with (a) bathymetric slope of**

442  $\frac{1}{450} \approx 0.002$  and (b) a simulation with a higher bathymetric slope ( $\frac{6}{450} \approx 0.013$ ). The upper part of each panel shows

443 the surface with the inundation water and the lower part is the vertical slice with the SLF values below the coastline

444 ( $X=450$  m).

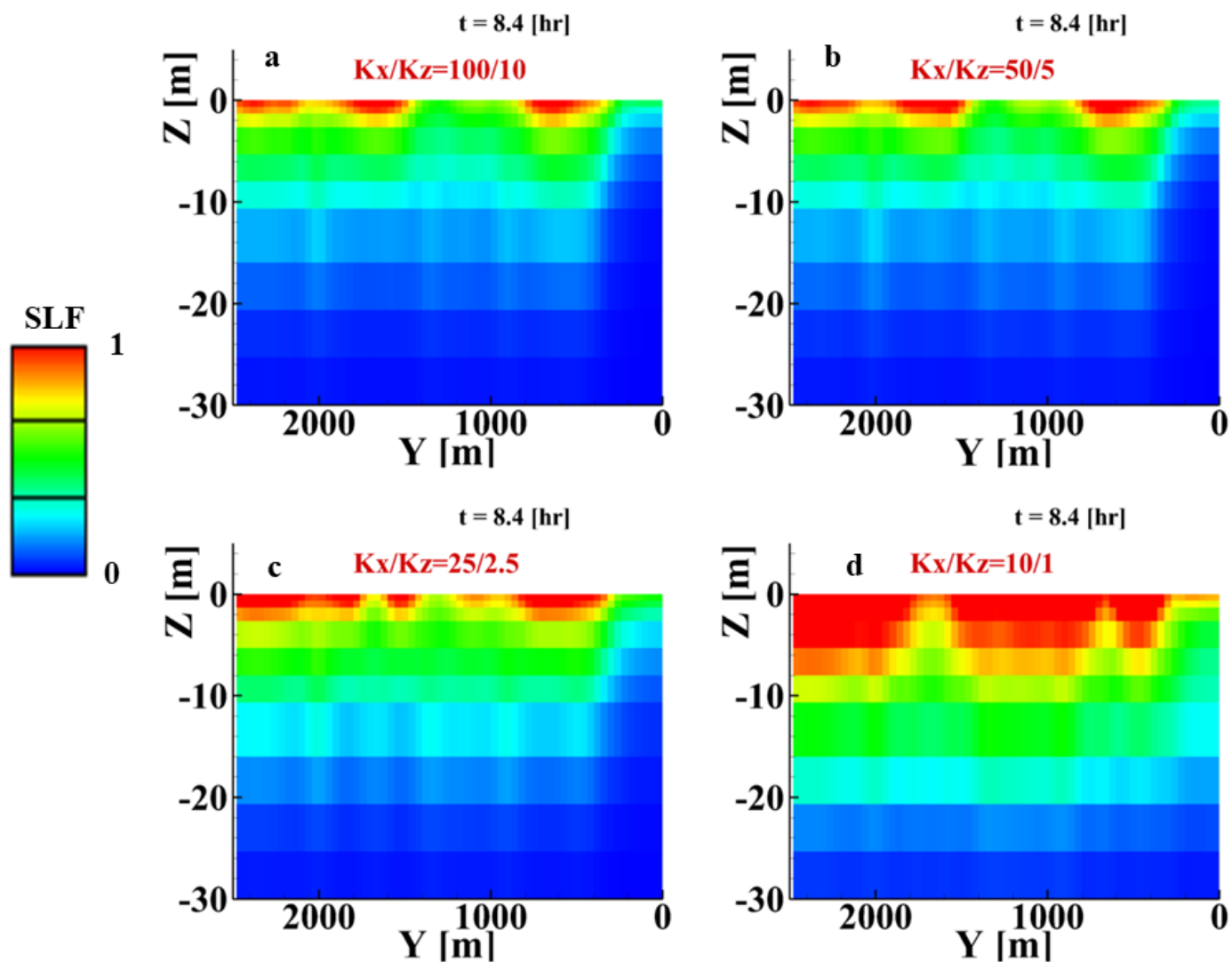
445



446

447 **Figure A3: Contours (color scales on the top) of vertical hydraulic gradients ( $i_z$ ) at  $X = 450 \text{ m}$  (shoreline location) for**  
448 **the pre-surge conditions (left) and the end of the surge when gradients are maximum (right) as a function of vertical  $Z$**   
449 **and alongshore  $Y$  coordinates. Note the different color scales between the pre-surge (left) and the peak (right) plots.**

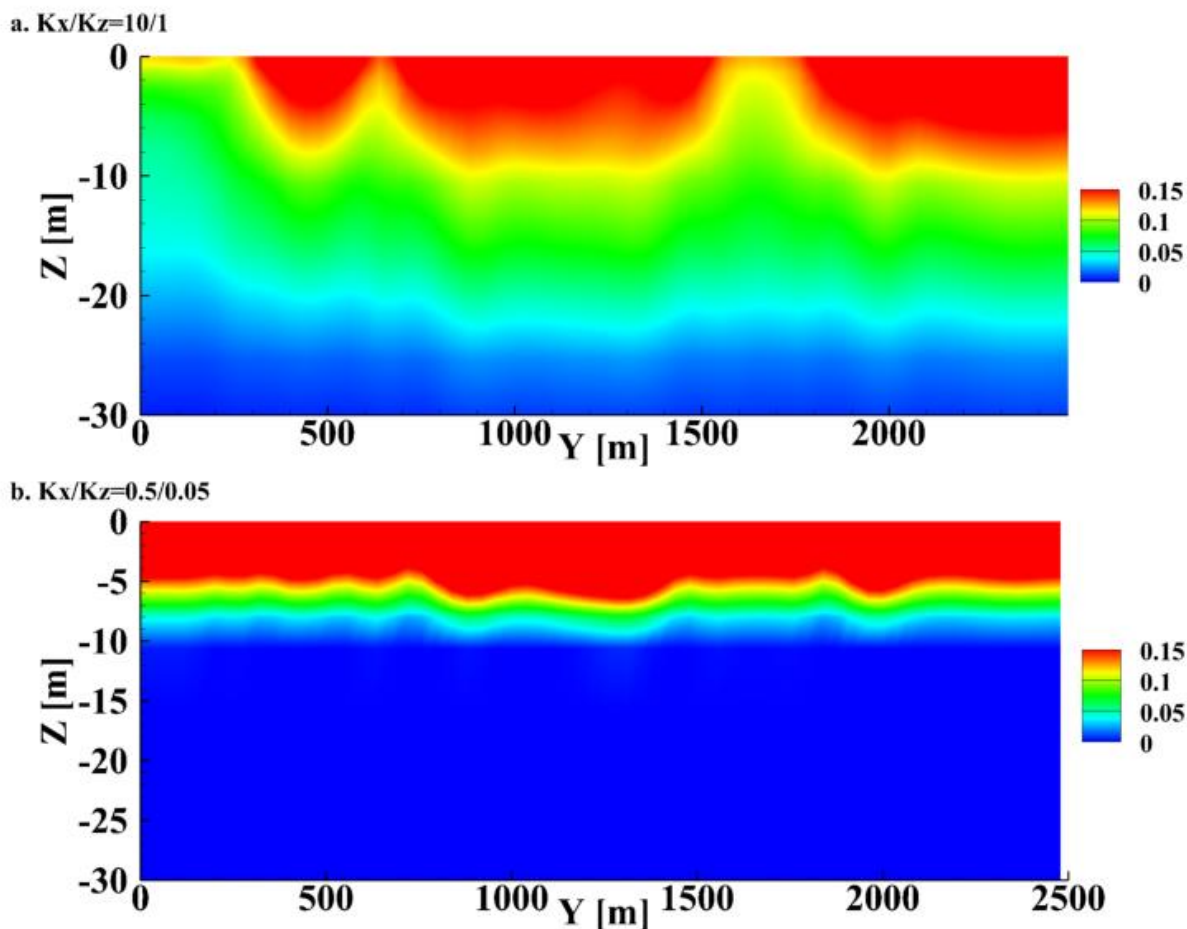
450



451

452 **Figure A4: Contours (color scale on the left) of peak SLF ( $t=8.4$  hr) vertical slices at the shoreline ( $X = 450$  m) for  $K_x$**   
453 **and  $K_z$  of (a) 100 and 10, (b) 50 and 5, (c) 25 and 2.5, and (d) 10 and 1 m/d.**

454



455  
456 **Figure A5: Contours (color scales on the right) of the maximum vertical hydraulic gradients ( $i_z$ ) at  $X = 450$  m (shoreline**  
457 **location) for (a)  $K_z = 1$  and (b)  $K_z = 0.05$  ) as a function of vertical  $Z$  and alongshore  $Y$  coordinates.**

458 **Author contribution**

459 AP: conceptualization, investigation, visualization, formal analysis, writing (original draft); NS: conceptualization, formal  
460 analysis, writing (review and editing), funding acquisition; MF: formal analysis, writing (review and editing); BR;  
461 conceptualization, formal analysis, writing (review and editing), funding acquisition; SE: conceptualization, formal analysis,  
462 writing (review and editing), funding acquisition; RH; Data curation, visualization, writing (review and editing); RF formal  
463 analysis, methodology; HM: conceptualization, formal analysis, writing (review and editing), supervision, funding acquisition,  
464 resources.



## 465 Acknowledgments

466 We thank the staff at the USACE Field Research Facility and the PVLAB field team for helping to deploy and maintain  
467 groundwater wells. Funding was provided by The National Science Foundation (OCE1848650, OIA1757353, OCE1829136,  
468 EAR1933010, CMMI-1751463, and a Graduate Research Fellowship), US Geological Survey (NIWR 2018DE01G), a  
469 Vannevar Bush Faculty Fellowship, the US Coastal Research Program, and the Woods Hole Oceanographic Institution  
470 Investment in Science Program.

## 471 References

- 472 Abdollahi, A., & Mason, H. B. (2020). Pore Water Pressure Response during Tsunami Loading. *Journal of Geotechnical and*  
473 *Geoenvironmental Engineering*. [https://doi.org/10.1061/\(asce\)gt.1943-5606.0002205](https://doi.org/10.1061/(asce)gt.1943-5606.0002205)
- 474 Ataie-Ashtiani, B., Werner, A. D., Simmons, C. T., Morgan, L. K., & Lu, C. (2013). How important is the impact of land-  
475 surface inundation on seawater intrusion caused by sea-level rise? *Hydrogeology Journal*. [https://doi.org/10.1007/s10040-013-](https://doi.org/10.1007/s10040-013-1021-0)  
476 [1021-0](https://doi.org/10.1007/s10040-013-1021-0)
- 477 Bratton, J. F. (2010). The Three Scales of Submarine Groundwater Flow and Discharge across Passive Continental Margins.  
478 *The Journal of Geology*, 118(5), 565–575. <https://doi.org/10.1086/655114>
- 479 Briaud, J.-L. (2013). *Geotechnical engineering: unsaturated and saturated soils*. John Wiley & Sons.
- 480 Burnett, W. C., Aggarwal, P. K., Aureli, A., Bokuniewicz, H., Cable, J. E., Charette, M. A., ... Turner, J. V. (2006).  
481 Quantifying submarine groundwater discharge in the coastal zone via multiple methods. *Science of the Total Environment*,  
482 367(2–3), 498–543. <https://doi.org/10.1016/j.scitotenv.2006.05.009>
- 483 Chini, N., & Stansby, P. K. K. (2012). Extreme values of coastal wave overtopping accounting for climate change and sea  
484 level rise. *Coastal Engineering*, 65, 27–37. <https://doi.org/10.1016/J.COASTALENG.2012.02.009>
- 485 ESRI. (2011). *ArcGIS Desktop: Release 10*. Redlands, CA: Environmental Systems Research Institute. Redlands.
- 486 Freeze, R. A., & Cherry, J. A. (1979). *Groundwater*. Prentice-Hall.
- 487 Gelhar, L. W., Welty, C., & Rehfeldt, K. R. (1992). A Critical Review of Data on Field-Scale Dispersin in Aquifers. *Water*  
488 *Resources Research*, 28(7), 1955–1974. <https://doi.org/10.1029/92WR00607>
- 489 Goren, L., Toussaint, R., Aharonov, E., Sparks, D. W., & Flekkøy, E. (2013). A general criterion for liquefaction in granular  
490 layers with heterogeneous pore pressure. In *Poromechanics V - Proceedings of the 5th Biot Conference on Poromechanics*.  
491 <https://doi.org/10.1061/9780784412992.049>
- 492 Guimond, J. A., & Michael, H. A. (2021). Effects of Marsh Migration on Flooding, Saltwater Intrusion, and Crop Yield in  
493 Coastal Agricultural Land Subject to Storm Surge Inundation. *Water Resources Research*, 57(2).  
494 <https://doi.org/10.1029/2020WR028326>
- 495 Housego, R., Raubenheimer, B., Elgar, S., Gorrell, L., Wadman, H., McNinch, J., & Brodie, K. (2018). BARRIER ISLAND  
496 GROUNDWATER. *Coastal Engineering Proceedings*. <https://doi.org/10.9753/icce.v36.risk.10>



- 497 Iverson, R. M. (1995). can magma-injection and groundwater forces cause massive landslides on Hawaiian volcanoes, 66,  
498 295–308.
- 499 Iverson, R. M., & Major, Jon J. (1986). Groundwater Seepage Vectors and the Potential for Hillslope Failure and Debris Flow  
500 Mobilization. *WATER RESOURCES RESEARCH*, 22(11), 1543–1548.
- 501 Iverson, R. M., & Reid, M. E. (1992). Gravity driven groundwater flow and slope failure potential: 1. Elastic Effective Stress  
502 Model. *Water Resources Research*, 28(3), 925–938. <https://doi.org/10.1029/91WR02694>
- 503 Mei, C. C., & Foda, M. A. (1981). Wave-induced responses in a fluid-filled poro-elastic solid with a free surface—a boundary  
504 layer theory. *Geophysical Journal of the Royal Astronomical Society*. <https://doi.org/10.1111/j.1365-246X.1981.tb04892.x>
- 505 Mory, M., Michallet, H., Bonjean, D., Piedra-Cueva, I., Barnoud, J. M., Foray, P., ... Breul, P. (2007). A field study of  
506 momentary liquefaction caused by waves around a coastal structure. *Journal of Waterway, Port, Coastal and Ocean*  
507 *Engineering*. [https://doi.org/10.1061/\(ASCE\)0733-950X\(2007\)133:1\(28\)](https://doi.org/10.1061/(ASCE)0733-950X(2007)133:1(28))
- 508 Orange, D. L., Anderson, R. S., & Breen, N. A. (1994). Regular Canyon Spacing in the Submarine Environment: The Link  
509 Between Hydrology and Geomorphology. *Geological Society of America Bulletin*, 4(2), 35–39.
- 510 Orange, D. L., Yun, J., Maher, N., Barry, J., & Greene, G. (2002). Tracking California seafloor seeps with bathymetry,  
511 backscatter and ROVs. *Continental Shelf Research*, 22(16), 2273–2290. [https://doi.org/10.1016/S0278-4343\(02\)00054-7](https://doi.org/10.1016/S0278-4343(02)00054-7)
- 512 Paldor, A., & Michael, H. A. (2021). Storm Surges Cause Simultaneous Salinization and Freshening of Coastal Aquifers,  
513 Exacerbated by Climate Change. *Water Resources Research*, 57(5), e2020WR029213.  
514 <https://doi.org/10.1029/2020WR029213>
- 515 Paldor, Anner, Aharonov, E., & Katz, O. (2020). Thermo-haline circulations in subsea confined aquifers produce saline,  
516 steady-state deep submarine groundwater discharge. *Journal of Hydrology*, 580. <https://doi.org/10.1016/j.jhydrol.2019.124276>
- 517 Rozhko, a. Y., Podladchikov, Y. Y., & Renard, F. (2007). Failure patterns caused by localized rise in pore-fluid overpressure  
518 and effective strength of rocks. *Geophysical Research Letters*, 34(22), L22304. <https://doi.org/10.1029/2007GL031696>
- 519 Sakai, T., Hatanaka, K., & Mase, H. (1992). Wave-induced effective stress in seabed and its momentary liquefaction. *Journal*  
520 *of Waterway, Port, Coastal and Ocean Engineering*, 118(2), 202–206. [https://doi.org/10.1061/\(ASCE\)0733-950X\(1992\)118:2\(202\)](https://doi.org/10.1061/(ASCE)0733-950X(1992)118:2(202))
- 521
- 522 Schorghofer, N., Jensen, B., Kudrolli, A., & Rothman, D. H. (2004). Spontaneous channelization in permeable ground: theory,  
523 experiment, and observation. *Journal of Fluid Mechanics*, 503(503), 357–374. <https://doi.org/10.1017/S0022112004007931>
- 524 Sous, D., Lambert, A., Rey, V., & Michallet, H. (2013). Swash-groundwater dynamics in a sandy beach laboratory experiment.  
525 *Coastal Engineering*. <https://doi.org/10.1016/j.coastaleng.2013.05.006>
- 526 Sous, D., Petitjean, L., Bouchette, F., Rey, V., Meulé, S., Sabatier, F., & Martins, K. (2016). Field evidence of swash  
527 groundwater circulation in the microtidal rocky beach, France. *Advances in Water Resources*.  
528 <https://doi.org/10.1016/j.advwatres.2016.09.009>
- 529 Stegmann, S., Sultan, N., Kopf, a., Apprioual, R., & Pelleau, P. (2011). Hydrogeology and its effect on slope stability along  
530 the coastal aquifer of Nice, France. *Marine Geology*, 280(1–4), 168–181. <https://doi.org/10.1016/j.margeo.2010.12.009>



- 531 Tebaldi, C., Strauss, B. H., & Zervas, C. E. (2012). Modelling sea level rise impacts on storm surges along US coasts.  
532 Environmental Research Letters. <https://doi.org/10.1088/1748-9326/7/1/014032>
- 533 Therrien, R., McLaren, R. G., Sudicky, E. A., & Panday, S. M. (2010). HydroGeoSphere. A three-dimensional numerical  
534 model describing fully-integrated subsurface and surface flow and solute transport. Groundwater Simulations Group.  
535 <https://doi.org/10.5123/S1679-49742014000300002>
- 536 Turner, I. L., Rau, G. C., Austin, M. J., & Andersen, M. S. (2016). Groundwater fluxes and flow paths within coastal barriers:  
537 Observations from a large-scale laboratory experiment (BARDEX II). Coastal Engineering.  
538 <https://doi.org/10.1016/j.coastaleng.2015.08.004>
- 539 Yang, J., Graf, T., Herold, M., & Ptak, T. (2013). Modelling the effects of tides and storm surges on coastal aquifers using a  
540 coupled surface-subsurface approach. Journal of Contaminant Hydrology, 149, 61–75.  
541 <https://doi.org/10.1016/j.jconhyd.2013.03.002>
- 542 Yang, J., Zhang, H., Yu, X., Graf, T., & Michael, H. A. (2018). Impact of hydrogeological factors on groundwater salinization  
543 due to ocean-surge inundation. Advances in Water Resources, 111, 423–434.  
544 <https://doi.org/10.1016/J.ADVWATRES.2017.11.017>
- 545 Yeh, H., & Mason, H. B. (2014). Sediment response to tsunami loading: Mechanisms and estimates. Geotechnique.  
546 <https://doi.org/10.1680/geot.13.P.033>
- 547 Yu, X., Yang, J., Graf, T., Koneshloo, M., O’Neal, M. A., & Michael, H. A. (2016). Impact of topography on groundwater  
548 salinization due to ocean surge inundation. Water Resources Research, 52(8), 5794–5812.  
549 <https://doi.org/10.1002/2016WR018814>
- 550 Zen, K., Jeng, D. S., Hsu, J. R. C., & Ohyama, T. (1998). Wave-induced seabed instability: Difference between liquefaction  
551 and shear failure. Soils and Foundations, 38(2), 37–47. [https://doi.org/10.3208/sandf.38.2\\_37](https://doi.org/10.3208/sandf.38.2_37)
- 552 Zinn, B., & Harvey, C. F. (2003). When good statistical models of aquifer heterogeneity go bad: A comparison of flow,  
553 dispersion, and mass transfer in connected and multivariate Gaussian hydraulic conductivity fields. Water Resources Research.  
554 <https://doi.org/10.1029/2001WR001146>
- 555